Arch. Metall. Mater. **67** (2022), 2, 637-643

DOI: https://doi.org/10.24425/amm.2022.137800

SHUYAN ZHANG[1,2*], ZHIBIN ZHANG[2], XIN WANG[2], YANGYANG GAO[1], XIUBING LIANG[2*]

EFFECTS OF YTTRIUM (Y) SUBSTITUTION BY CERIUM (Ce) ON MICROSTRUCTURE AND CORROSION BEHAVIOR OF NEAR-EQUIATOMIC ALNIY MEDIUM-ENTROPY AMORPHOUS ALLOY RIBBONS

Through partially replacing Y element, Ce was added into near-equiatomic AlNiY medium-entropy amorphous alloy (denoted as MEAA) ribbons by the melt spinning process in this study. The differences of microstructure, thermal stability, hardness and corrosion resistance of $Al_{33.3}Ni_{33.3}Y_{33.4-x}Ce_x$ (x = 0, 2, 5, 8, 13) alloy ribbons were investigated by X-ray diffraction (XRD), scanning electron microscope (SEM), differential scanning calorimeter (DSC) and Vickers-type hardness tester. The anti-corrosion performance in 3.5 wt.% NaCl solution of alloy ribbons was investigated elaborately through the general potentiodynamic polarization curves (Tafel) and electrochemical impedance spectroscopy (EIS). Results suggested that all ribbon samples could remain amorphous structure and the hardness are all above 510 $HV_{0.1}$. With the increase of Ce content, the thermal stability begins to be gradually lower. However, according to the analysis of crystallization kinetics, all types of MEAA ribbons presents the relatively prominent thermal stability compared with traditional Al-based amorphous alloys. The corrosion current density raises firstly, then shows a decreasing trend, and has a slight increase at last. Therefore, appropriate content of Ce element can improve the corrosion protection performance of alloy ribbons and the 5 at.% Ce MEAA ribbons exhibited the excellent corrosion resistance in this study.

Keywords: Medium-entropy amorphous alloys; Corrosion behavior; Thermal stability analysis; Microstructure; Cerium content

1. Introduction

Due to the lack of translational or orientational long-range order and crystalline defects, metallic glasses generally have prominent properties including high hardness, exceptional wear and corrosion resistance, superb mechanical strength, and wildly applied as anti-corrosion and wear-resistant materials, which is different from their crystalline counterparts [1-3]. These unusual structural and functional properties can be attributed to the unique disordered structure, metastable state and tunable compositions of metallic glasses and thus become a hot spot in the frontier field of glass science and applications [4-6]. In order to fabricate metallic glasses, researchers produced them directly from the liquid state during cooling so as to prevent the nucleation and growth of crystals. The rapid cooling is too fast for crystals to form (for example 10^3 K or above) and the material seems "locked in" a glassy state. Over the past decades, a few approaches have been developed for different forms of amorphous alloys (such as bulk, ribbons, coatings, powder, plates, etc.), which include copper-mold suction casting, single roll quenching, gas atomization, thermal-sprayed forming, mechanical alloying and powder consolidation techniques [7-9].

High-entropy alloys, a new class of cutting-edge advanced materials with novel alloy design concept, consists of five or more principal elements in relatively high concentrations (5~™at.%) compared to conventional alloys based on one or at most two principal elements [10,11]. High-entropy alloys also possess promising properties, for instance, excellent strength and ductility combinations, anti-corrosion and wear resistance, in virtue of four core effects, namely, high-entropy effect, sluggish diffusion, lattice distortion and cocktail effect [12,13]. Over the past five years, increased attention has been paid because of their outstanding functional properties and a myriad of potential applications, such as soft magnetic properties, superconducting behavior, thermoelectric performance and a potential candidate for high-temperature applications [14,15].

However, in order to acquire the alloys with high cost performance, some research groups developed medium-entropy alloys based on three or four principal elements by tailoring chemical composition, which can also meet the required proper-

[1] ZHEJIANG UNIVERSITY, OCEAN COLLEGE, ZHOUSHAN 316021, PEOPLES REPUBLIC OF CHINA
[2] DEFENSE INNOVATION INSTITUTE, ACADEMY OF MILITARY SCIENCES OF THE PLA OF CHINA, BEIJING 100071, PEOPLES REPUBLIC OF CHINA
* Corresponding authors: zsy19930524@sina.com; liangxb_d@163.com

ties [16]. Corrosion behavior of metal materials in severe marine environment is a complex physical and chemical process, which is mainly influenced by high temperature, high humidity, intensive ultraviolet radiation and cyclic wet-dry salt fog conditions. Thus, it is of great value to blossom out novel metal materials with superb corrosion protection performance and desired mechanical properties under the condition of harsh marine climate. Zhang et al. [17] pointed out that the corrosion resistance of micro-alloyed steels in 3.5 wt.% NaCl solution became higher after addition of cerium element. Ce addition reduced the surface electrochemical activity, leading to a less adsorption tendency of Cl^- on the metal surface. Similar conclusions had been reached by Zhang et al. [18] as well. They explored the effect of Ce content on the anti-corrosion performance of Al-Co-Ce amorphous alloys in 0.6 M NaCl solution. It was found that appropriate Ce content addition is responsible for the improvement of corrosion resistance by the formation of a more protective adhered passive film on the alloys and reducing the localized attack promoted via pitting. By contrast, adding excess Ce can result in the reduced corrosion resistance. Baroni et al. [19] also presented there is a threshold in Fe-Mn-Si-based shape memory stainless steel where Ce element starts to be detrimental. In view of the above analysis, the plan of this research is to investigate the effect of partial replacement of yttrium element by cerium on microstructure and corrosion resistance of novel near-equiatomic AlNiY MEAA ribbons.

2. Materials and methods

2.1. Alloy ribbons preparation

The alloy ingots were prepared from pure elemental Al, Ni, Y and Ce of 99.9 mass% purity (Linyi Innovative Materials Technology Co., Ltd., Shandong Province, China) by arc melting process in a Ti-gettered high purity argon atmosphere. In order to achieve good alloy compositional homogeneity, the alloy button need to be flipped and re-melted at least five times under the heating current of below 180 A. $Al_{33.3}Ni_{33.3}Y_{33.4-x}Ce_x$ ($x = 0, 2, 5, 8, 13$) MEAA ribbons were fabricated by subsequently injected the molten master alloy onto a rotating copper roller (3300 r/min) with a copper-wheel surface velocity of 30 m/s under a purified argon atmosphere. The generated ribbons having no noticeable porosities were 1.5~2.0 mm wide and 30~40 mm thick, and a density of 4.8~5.4 g/cm^3.

2.2. Structural characterization

The surface morphology and chemical compositions of the specimens were observed by scanning electron microscope (SEM, Zeiss Gemini 300) and energy dispersive X-ray spectroscopy (EDS). Images were obtained at an operating voltage of 3.00 kV and the working distance was ranging from 7.7 mm to 13.4 mm. The amorphous structure of specimens were confirmed by an Empyrean X-ray diffractometer (XRD, PANAnalytical, Netherlands) using monochromatic Cu-Kα radiation ($\lambda = 0.15406$ nm) at an accelerating voltage of 40 kV and a current of 40 mA. The original samples were scanned in the typical range $2\theta = 20° \sim 80°$ at a scan rate of 5°/min.

2.3. Thermal stability and hardness test

The thermal stability of the MEAA ribbons was analyzed by a differential scanning calorimeter (DSC, NETZSCH 404F3) at a heating rate of 20 K/min under a flow of high purity argon using Al_2O_3 crucibles. In the meantime, the dynamic thermal treatment ranges from 400 K to 1000 K with the heating speeds of 10, 20, 30 and 40 K/min for the purpose of the discovery regarding crystallization kinetics of these alloy ribbons. The Vickers microhardness of these rapidly solidified ribbons were ascertained by a Vickers-type hardness tester (HVS-1000A, Huayin, Laizhou, China), under a load of 0.98 N and a duration time of 10 s.

2.4. Electrochemical measurements

Corrosion behavior of ribbon samples was characterized by electrochemical workstation (CHI 660E, Chenhua, Shanghai) in the 3.5 wt.% NaCl solution. Potentiodynamic polarization curves were performed in a typical three-electrode cell setup when the open-circuit potentials became almost steady at room temperature and the specimens were tested at a scan rate of 0.01 V/s from the initial potential of –0.5 V vs SCE (saturated calomel electrode). The surface area of specimens (i.e. the shiny side of the ribbons) exposed to solutions ranged from 0.45 to 0.50 cm^2. For EIS measurements, a 5 mV rms of sinusoidal perturbation was utilized from 10^5 Hz down to 10^{-1} Hz at 10 points per frequency decade. An equivalent circuit was analyzed through the ZSimpWin software to further delve into the impedance spectra of the corrosion behavior in chloride. Each measurement need to be repeated at least three times under the same condition to ensure the reliability of data.

3. Results and discussion

3.1. Microstructural characterization

Fig. 1 shows the SEM micrographs of these MEAA ribbons with various Ce content. As can be seen from these figures, there was no evidence of segregation or phases on the MEAA ribbon surface, which is quite smooth and whose chemical elements were evenly distributed without there being any preferential location. This is mainly because the melt spinning route hinders grain formation owing to the higher cooling rate [20].

X-ray diffraction patterns of the melt-spun MEAA ribbons with different cerium contents were illustrated in Fig. 2. It can

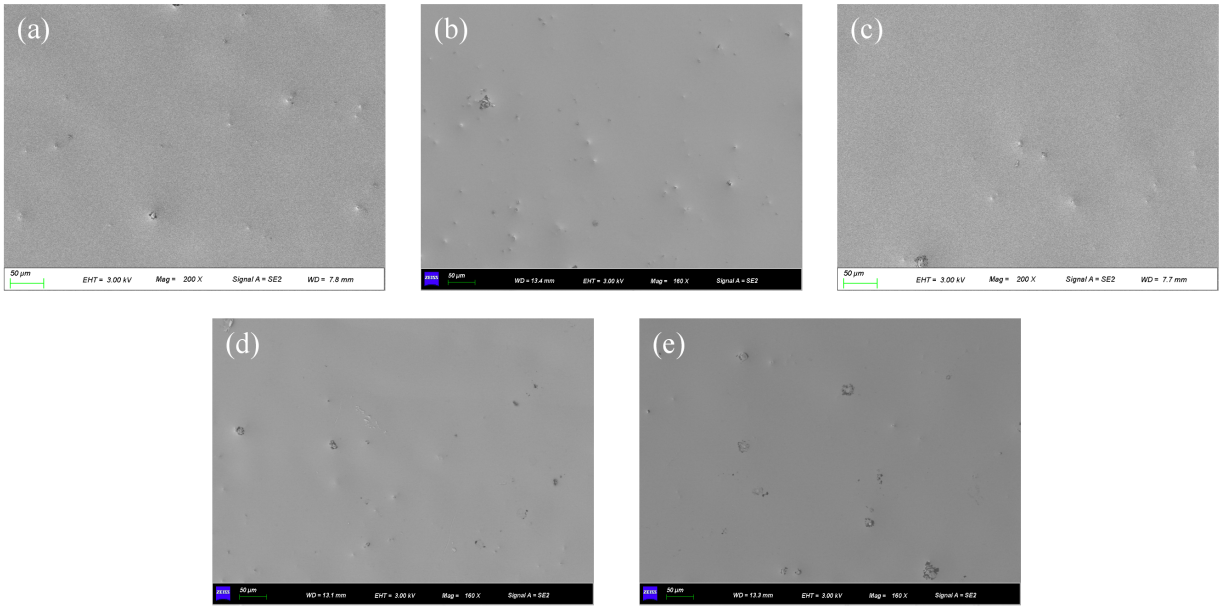

Fig. 1. SEM micrographs (a)-(e) of the $Al_{33.3}Ni_{33.3}Y_{33.4-x}Ce_x$ (x = 0, 2, 5, 8, 13) melt-spun MEAA ribbons

be seen from the figure that all diffraction profiles primarily consist of a typical broad diffraction peak and none of appreciable diffraction peaks coincident with crystalline phase can be observed. This is due to the simple fact that the growth and even nucleation of crystalline phases are slightly inhibited for the sluggish diffusion effect in the medium- and high-entropy alloys, and alloys with a typical amorphous state were obtained possibly using rapid solidification process [21,22].

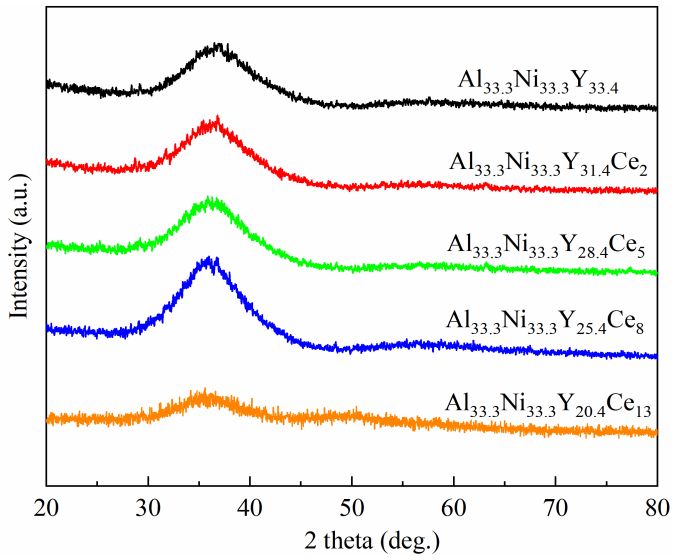

Fig. 2. XRD patterns of the $Al_{33.3}Ni_{33.3}Y_{33.4-x}Ce_x$ (x = 0, 2, 5, 8, 13) melt-spun MEAA ribbons

3.2. Thermal stability, non-isothermal crystallization kinetics and hardness test

In order to study the thermal stability of the $Al_{33.3}Ni_{33.3}Y_{33.4-x}Ce_x$ (x = 0, 2, 5, 8, 13) melt-spun MEAA ribbons, DSC curves were recorded during continuous heating at a rate of 20 K/min. As is seen in Fig. 3, the partial replacement of Y element by Ce significantly changes the crystallization process of the previous counterpart. In the meantime, sharp exothermic peak related to crystallization can be detected in the DSC traces of the alloy ribbons, which further confirms their fully glassy structure. The DSC traces corresponding to five kinds of MEAA ribbons exhibited two separated exothermic peaks, namely, an obvious peak and a faint visible peak with the increasing position, indicating that structural transformation into the final phases occurs in two steps, combined with the first derivative of DSC experimental data in Fig. 4. These typical physical features of crystallization processes is similar with the previous research regarding the thermal stability analysis of $Al_{84}Ni_8Ce_5M_3$ (M = Fe, Co) and finally transform a representative primary crystallization of fcc-Al phase to a eutectic crystallization [23]. Note that the first exothermic peak moves forward with an increasing Ce addition. In contrast, the second peak becomes becomes shallower and weaker. Thus, the temperature interval between the first and second peaks consequently enlarges.

However, like most Al-based amorphous alloys, no evident glass transition temperature (T_g) is observed prior to the onset crystallization temperature (T_x) that can be caused by the presence of quench-in nuclei or faint thermal signal connected with glass transition temperature [24]. That is to say, for certain alloy systems T_x precedes T_g, the endothermic peak could not be observed since crystallization happen first [25]. The high onset crystallization temperature above 660 K indicates an exceptional thermal stability of the alloys, which put down to the high mixed entropy effect. The T_x and two crystallization peak temperatures (T_{p1} and T_{p2}) under the common heating rate of 20 K/min are listed in TABLE 1. It can be indicated that the T_x is strongly dependent on alloy compositions and descends distinctly with the increase of Ce content. To be more specific, T_x decreased from

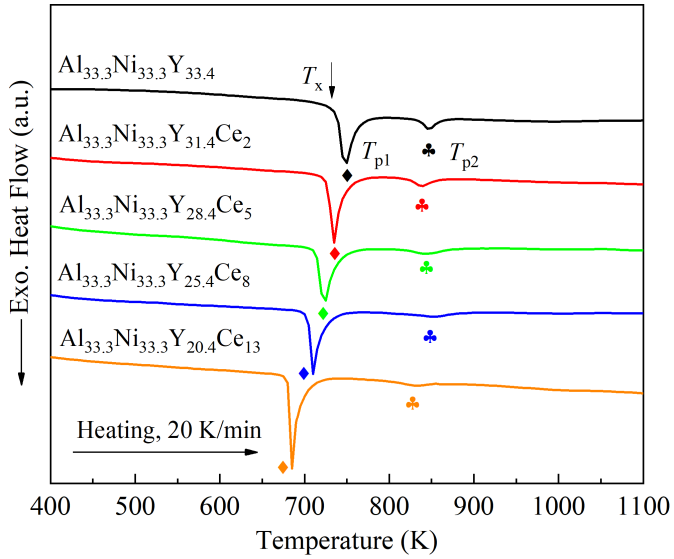

Fig. 3. DSC curves of the $Al_{33.3}Ni_{33.3}Y_{33.4-x}Ce_x$ ($x = 0, 2, 5, 8, 13$) melt-spun MEAA ribbons

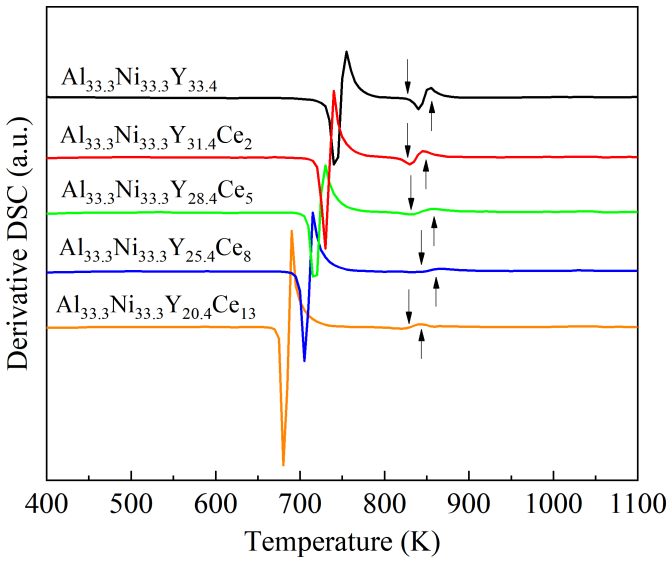

Fig. 4. DDSC curves of the $Al_{33.3}Ni_{33.3}Y_{33.4-x}Ce_x$ ($x = 0, 2, 5, 8, 13$) melt-spun MEAA ribbons

720 K for $Al_{33.3}Ni_{33.3}Y_{33.4}$ to 669 K for $Al_{33.3}Ni_{33.3}Y_{20.4}Ce_{13}$. This phenomenon looks as if it ought to put down to the lower melting point of cerium and its vital role in glass formation in the Al-Ni-Y-Ce alloy system, which pares down that of alloys and the thermal characteristics.

Meanwhile, crystallization kinetic analysis for these alloy ribbons were performed by calculating the activation energy through Kissinger method as well, which represents an important kinetic parameter [26]. It is widely employed because of its greater speed and convenience in comparison with the isothermal analysis. According to the following equation:

$$\ln\left(\frac{\beta}{T^2}\right) = -\frac{E}{RT} + C \qquad (1)$$

where β represents the heating rate, R is the gas constant, T refers to a specific temperature such as the onset crystallization temperature T_x or the peak temperature T_p, E denotes the activation energy, C corresponds to a temperature-independent constant. In our current study, the first crystallization peak temperature T_{p1} is applied to estimate the activation energy for crystallization of five MEAA ribbons because of much subtler error in determining T_{p1} than T_x. Fig. 5 was a Kissinger plot of $\ln(\beta/T^2)$ versus $1000/T$ yields an approximate straight line with a slope of E/R, from which crystallization activation energy E_{p1} can be deduced and the activation energies for crystallization are also tabulated in TABLE 1. This means that the activation energy for the first crystallization reactions were influenced by alloy composition. The higher value of activation energy for crystallization in Al-Ni-Y-Ce alloys, compared with other Al-based amorphous alloys, for instance, $Al_{83}Ni_{10}Si_2Ce_5$, $Al_{87}Ni_5Co_2Nd_6$ and $Al_{85}Ni_{10}Ce_5$ amorphous alloys, also implies the much higher thermal stability of MEAA ribbons [27].

In general, wear resistance is closely allied to the hardness of the metal material [28]. Fig. 6 is the hardness of the ribbon

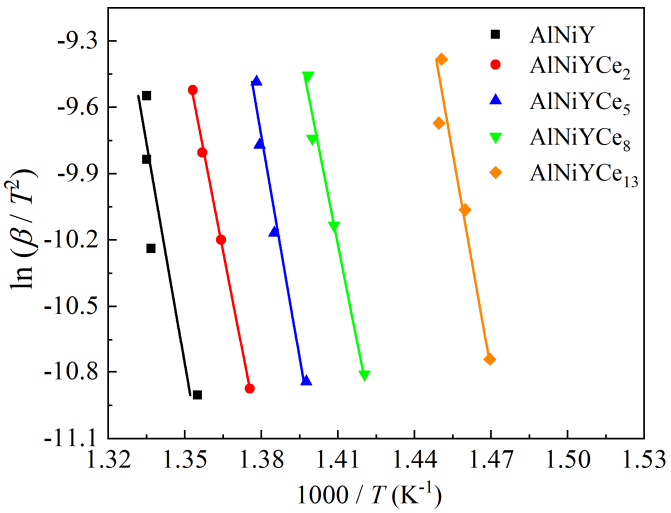

Fig. 5. Kissinger plots for the $Al_{33.3}Ni_{33.3}Y_{33.4-x}Ce_x$ ($x = 0, 2, 5, 8, 13$) melt-spun MEAA ribbons

TABLE 1

The thermal parameters of Al-Ni-Y-Ce alloys under the heating rate of 20 K/min and their crystallization activation energy E_{p1}

Samples	T_x /K	T_{p1} /K	T_{p2} /K	E_{p1} (kJ/mol)
$Al_{33.3}Ni_{33.3}Y_{33.4}$	720	748	847	553.9±7.4
$Al_{33.3}Ni_{33.3}Y_{31.4}Ce_2$	716	733	838	495.5±13.7
$Al_{33.3}Ni_{33.3}Y_{28.4}Ce_5$	698	722	845	556.9±10.2
$Al_{33.3}Ni_{33.3}Y_{25.4}Ce_8$	692	710	853	486.8±9.5
$Al_{33.3}Ni_{33.3}Y_{20.4}Ce_{13}$	669	685	832	544.5±8.8

samples with different cerium content. It is shown that the hardness of them is all above 510 $HV_{0.1}$, which is about two times as hard as common Al-Ni-Y-based amorphous alloys, for example $Al_{86}Ni_6Co_2Y_{2.5}La_{1.5}Ce_2$ and $Al_{86}Ni_6Y_6Ce_2$ alloy ribbons. This phenomenon is likely to lie in the high mixed entropy which stabilizes the amorphous nature with enhanced homogeneity [29].

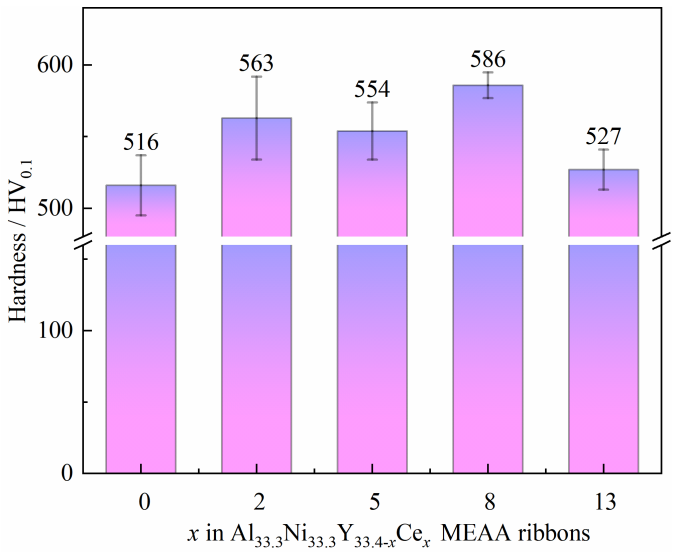

Fig. 6. Hardness of the $Al_{33.3}Ni_{33.3}Y_{33.4-x}Ce_x$ (x = 0, 2, 5, 8, 13) melt-spun MEAA ribbons

3.3. Electrochemical corrosion behavior

3.3.1. Potentiodynamic polarization measurement

The typical potentiodynamic polarization curves for the melt-spun ribbon samples soaked in 3.5 wt.% NaCl solution at room temperature are provided in Fig. 7. The corrosion potential (E_{corr}) and current density (i_{corr}) from the potentiodynamic polarization curves are gathered in Table 2. And some of the related corrosion electrochemical parameters obtained by fitting the polarization data, such as the cathodic (β_c), anodic (β_a) slops and the polarization resistance (R_p) can also be displayed in the table. It is noteworthy, with the increase of Ce content, the corrosion current density of these ribbons increased initially, followed by a decrease, but then again increased slight. From the polarization curves and the data in TABLE 2, the corrosion potential for $Al_{33.3}Ni_{33.3}Y_{33.4-x}Ce_x$ (x = 2, 8, 13) alloys is much higher than that of near-equiatomic AlNiY alloys, suggesting a lower corrosion tendency of these alloys in comparison with $Al_{33.3}Ni_{33.3}Y_{33.4}$ alloys [30]. In spite of the fact that $Al_{33.3}Ni_{33.3}Y_{28.4}Ce_5$ MEAA ribbon revealed the lowest corrosion potential, however, among the five Al-Ni-Y-based alloy samples, it also owned the lowest corrosion current density and the highest polarization resistance, viz., a stable value approximately at 6.4×10^{-7} A/cm^2 and 56.9 kΩ·cm^2. It can also demonstrate that the actual corrosion rate of $Al_{33.3}Ni_{33.3}Y_{28.4}Ce_5$ alloys is the slowest in 3.5 wt.% NaCl solution.

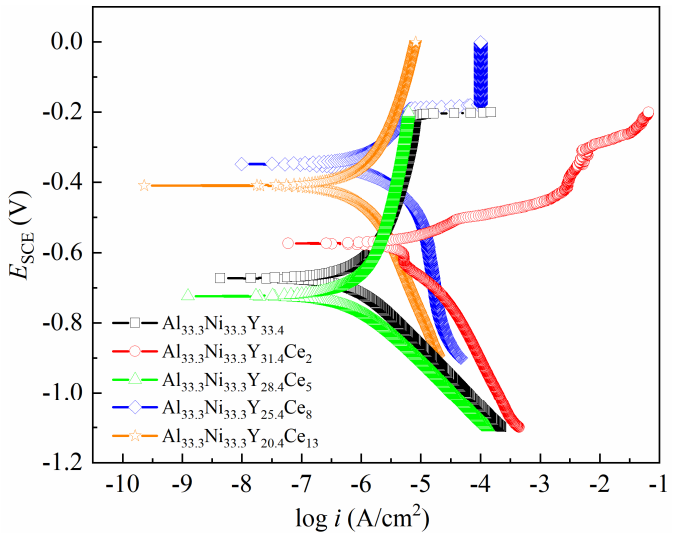

Fig. 7. Potentiodynamic polarization curves of the $Al_{33.3}Ni_{33.3}Y_{33.4-x}Ce_x$ (x = 0, 2, 5, 8, 13) melt-spun MEAA ribbons

3.3.2. EIS study

Electrochemical impedance analysis is a vital approach to reveal the electrochemical processes occurred on the surface [31]. On account of the poorer anti-corrosion property of $Al_{33.3}Ni_{33.3}Y_{31.4}Ce_2$ MEAA ribbons, EIS measurements were conducted in 3.5 wt.% NaCl solution to specifically evaluate the corrosion behaviors of the other four MEAA ribbon samples. Fig. 8a and 8b presents the Nyquist plots and Bode plots of the $Al_{33.3}Ni_{33.3}Y_{33.4-x}Ce_x$ (x = 0, 5, 8, 13) ribbon alloys. The insert plot in Fig. 8a is the equivalent electrical circuit used to fit experimental impedance spectra. For the near-equiatomic AlNiY alloy and Ce-added AlNiY-based MEAA ribbons, the Nyquist plots are made up of depressed capacitive semicircle in the high-frequency region. The asymmetric shape of these semicircles is main feature of a frequency dispersion that can be attributed to physical phenomena related to electrode roughness, the distribution of surface-active sites and the non-homogeneity of the electrode surfaces [32,33]. Taken such behavior into account, it is more appropriate to apply constant phase elements (CPEs) rather than ideal capacitors in the equivalent circuit models to fit

TABLE 2

The electrochemical parameters of the ribbons estimated from polarization curves data in 3.5 wt.% NaCl solution

Samples	E_{corr} /V_{SCE}	I_{corr} /μA·cm^{-2}	R_p /kΩ·cm^2	β_a mV·dec^{-1}	β_c mV·dec^{-1}
$Al_{33.3}Ni_{33.3}Y_{33.4}$	–0.67±0.02	0.78±0.09	48.3±0.2	211±5	147±4
$Al_{33.3}Ni_{33.3}Y_{31.4}C_{e2}$	–0.57±0.03	6.19±0.11	3.2±0.1	72±6	127±4
$Al_{33.3}Ni_{33.3}Y_{28.4}C_{e5}$	–0.72±0.04	0.64±0.12	56.9±0.3	234±8	131±7
$Al_{33.3}Ni_{33.3}Y_{25.4}Ce_8$	–0.35±0.03	1.56±0.08	24.0±0.2	189±6	159±5
$Al_{33.3}Ni_{33.3}Y_{20.4}Ce_{13}$	–0.41±0.04	0.85±0.10	52.6±0.1	206±7	204±6

the experimental data. Moreover, accompanied with the increasing quantity of Ce element, the radius of semicircular arcs raises firstly and then decreases. To go a further step, in comparison with Ce-free AlNiY medium-entropy amorphous alloys, the radius size of impedance spectra exhibits an increasing trend and implies the enhancement in the anti-corrosion performance by means of the appropriate addition of Ce element.

The proposed equivalent electric circuits that satisfactorily resolves the experimental results of electrochemical impedance are exhibited in the inset of Fig. 8a, and the fitted parameters in accordance with the model in the current study are set out in TABLE 3. In the circuits, R_s stands for solution resistance. The parallel-connected elements contain the constant phase element (CPE) and charge transfer resistance (R_{ct}), which are commonly used to describe the electrochemical procedure at the surface film-substrate interface [34]. The CPE was used to depict the homogeneity of the passive layer and to weigh up the ability to accumulate an electric charge on the material/electrolyte interface [35]. The impedance of CPE can be defined as $Z_{CPE} = [(Q(j\omega)^n]^{-1}$, where Q is the CPE magnitude, j is the imaginary number ($j^2 = -1$), ω is the angular frequency, and n is CPE exponent determined by the presence of surface roughness and defects that bring about inhomogeneous current distributions [36]. Considering the allowable error range of the experimental results, except $Al_{33.3}Ni_{33.3}Y_{25.4}Ce_8$ MEAA ribbons, the other three samples exhibits higher R_{ct} (>5.8×10^4 Ω cm^2) according to TABLE 2. Generally speaking, smaller charge transfer resistance signifies higher corrosion rate and poorer anti-corrosion performance. Hence, AlNiY medium-entropy amorphous alloys containing moderate cerium content can conduce to the improvement of corrosion resistance. Combined with the data from TABLE 2 and TABLE 3, $Al_{33.3}Ni_{33.3}Y_{33.4-x}Ce_x$ (x = 0, 5, 13) MEAA ribbons having favourable corrosion resistance is manifested clearly. In addition, in consideration of the hardness results of alloy ribbons, $Al_{33.3}Ni_{33.3}Y_{28.4}Ce_5$ MEAA ribbons have the most optimal corrosion resistance and superior wear-resisting potential performance within the scope of this study, thereby broadening the alloy application prospects.

4. Conclusions

In summary, the thermal stability and anti-corrosion property of the $Al_{33.3}Ni_{33.3}Y_{33.4-x}Ce_x$ (x = 0, 2, 5, 8, 13) MEAA ribbons were studied. The phase structure and microstructure of alloy ribbons were discussed by using XRD and SEM/EDS analyses. The conclusions in this current research were as follows:

(1) Melt-spun Al-Ni-Y-based medium-entropy amorphous alloy ribbons by partial replacement of yttrium with cerium element are completely amorphous structure.

(2) With increased content of Ce content, the thermal stability of $Al_{33.3}Ni_{33.3}Y_{33.4-x}Ce_x$ (x = 0, 2, 5, 8, 13) alloy ribbons decreases by reason of the reduction of MEAA melting point. However, the higher value of activation energy for crystallization in Al-Ni-Y-Ce alloy ribbons indicates their exceptional thermal stability, compared with conventional Al-based amorphous alloys.

TABLE 3

Fitting parameter values obtained from impedance measurements for melt-spun MEAA ribbons

Sample	R_s (Ω·cm^2)	CPE (S·cm^{-2}·s^n)	n	R_{ct} (Ω·cm^2)	Error (%)
$Al_{33.3}Ni_{33.3}Y_{33.4}$	2.86±0.07	(6.35±0.30)×10^{-6}	(0.928±0.015)	(5.84±0.03)×10^4	4.426
$Al_{33.3}Ni_{33.3}Y_{30.4}Ce_5$	3.02±0.08	(6.43±0.25)×10^{-6}	(0.927±0.014)	(6.46±0.04)×10^4	4.014
$Al_{33.3}Ni_{33.3}Y_{25.4}Ce_8$	2.65±0.09	(7.93±0.27)×10^{-6}	(0.901±0.018)	(4.69±0.03)×10^4	7.404
$Al_{33.3}Ni_{33.3}Y_{20.4}Ce_{13}$	6.50±0.11	(9.35±0.28)×10^{-6}	(0.779±0.025)	(7.74±0.06)×10^4	6.819

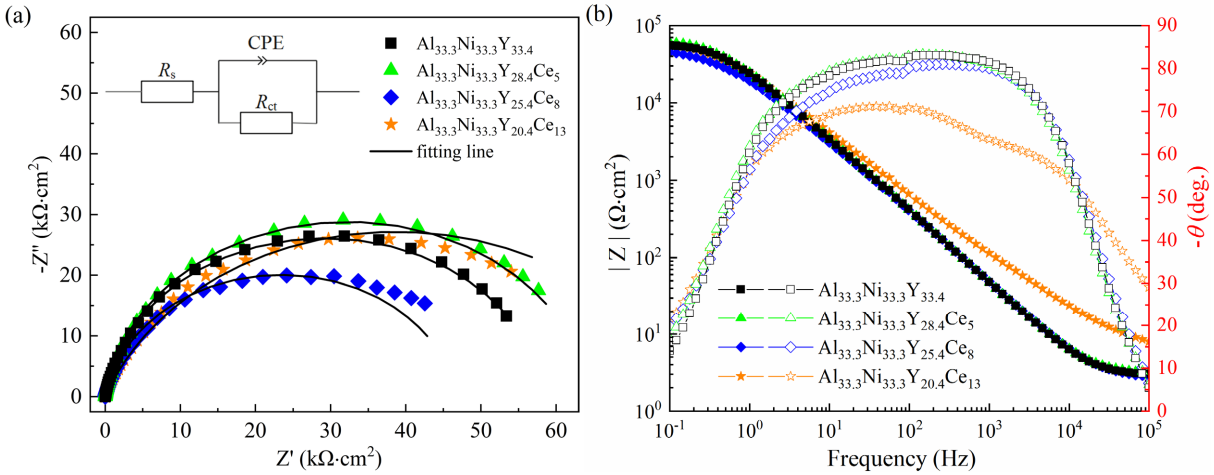

Fig. 8. EIS spectra acquired for the $Al_{33.3}Ni_{33.3}Y_{33.4-x}Ce_x$ (x = 0, 5, 8, 13) melt-spun MEAA ribbons in 3.5 wt.% NaCl solution (a) Nyquist plots, (b) Bode plots. The inset of Fig. 8a shows the equivalent electric circuit used for analyzing EIS data

(3) The addition of moderate cerium content can be propitious to enhance the corrosion resistance of near-equiatomic Al-NiY medium-entropy amorphous alloys. Nonetheless, it is noteworthy that the exact addition or partial replacement of cerium content needs to be digged into the future research at great length on the basis of diverse alloy systems.

Declaration of competing interest

The authors declare that they have no known competing financial interests or personal relationships that could have appeared to influence the work reported in this paper.

Acknowledgment

The authors would like to thank WEIWEI WANG and LU HUANG from Shiyanjia Lab (www.shiyanjia.com) for the XRD and SEM/EDS characterization. The authors also appreciate that Prof. BAOLONG SHEN and Dr. CHANGJIU CHEN from China University of Mining and Technology have provided the alloy preparation site for our study.

Funding

This project was supported by the National Key Research and Development Program of China (Grant No. 2018YFC1902400) and National Natural Science Foundation of China (Grant No. 51975582).

REFERENCES

[1] H.X. Li, Z.C. Lu, S.L. Wang, Y. Wu, Z.P. Lu, Prog. Mater. Sci. **103**, 235 (2019).
[2] Z. Li, Z. Huang, F. Sun, X. Li, J. Ma, Mater. Today Adv. **7**, 100077 (2020).
[3] F.C. Li, T. Liu, J.Y. Zhang, S. Shuang, Q. Wang, A.D. Wang, J.G. Wang, Y. Yang, Mater. Today Adv. **4**, 100027 (2019).
[4] W.H. Wang, Prog. Mater. Sci. **106**, 100561 (2019).
[5] Y.C. Hu, C. Sun, C. Sun, ChemCatChem. **11,** 2401 (2019).
[6] B. Huang, C. Zhang, G. Zhang, H. Liao, Surf. Coat. Technol. **377,** 124896 (2019).
[7] J.C. Huang, J.P. Chu, J.S.C. Jang, Intermetallics **17**, 973 (2009).
[8] E. Axinte, Mater. Des. **32**, 1717 (2011).
[9] J. Qiao, H. Jia, P.K. Liaw, Mater. Sci. Eng. R Rep. **100**, 1 (2016).
[10] J.W. Yeh, S.K. Chen, S.J. Lin, J.Y. Gan, T.S. Chin, T.T. Shun, C.H. Tsau, S.Y. Chang, Adv. Eng. Mater. **6**, 299 (2004).
[11] D.B. Miracle, O.N. Senkov, Acta Mater. **122**, 448 (2017).
[12] E.J. Pickering, N.G. Jones, Int. Mater. Rev. **61**, 183 (2016).
[13] R.B. Nair, H.S. Arora, A. Ayyagari, S. Mukherjee, H.S. Grewal, Adv. Eng. Mater. **20**, 1700946 (2018).
[14] S. Praveen, H.S. Kim, Adv. Eng. Mater. **20**, 1700645 (2018).
[15] M.C. Gao, D.B. Miracle, D. Maurice, X. Yan, Y. Zhang, J.A. Hawk, J. Mater. Res. **33**, 3138 (2018).
[16] J. Yi, X. Zhuang, J. He, M. He, W. Liu, S. Wang, Corros. Sci. **189**, 109628 (2021).
[17] S. Zhang, J. Liu, M. Tang, X. Zhang, K. Wu, J. Mater. Res. Technol. **11**, 519 (2021).
[18] L.M. Zhang, S.D. Zhang, A.L. Ma, A.J. Umoh, H.X. Hu, Y.G. Zheng, B.J. Yang, J.Q. Wang, J. Mater. Sci. Technol. **35**, 1378 (2019).
[19] L.F.S. Baroni, R. Silva, G.S. Vacchi, V.L. Sordi, C.A.D. Rovere, Mater. Today Commun. **25**, 101649 (2020).
[20] E. Galindo, A. Covelo, R. González-Parra, A. Tejeda, M. Hernández, Mater. Lett. **302**, 130389 (2021).
[21] Y.F. Ye, Q. Wang, J. Lu, C.T. Liu, Y. Yang, Mater. Today **19**, 349 (2016).
[22] L. Xue, L. Shao, Q. Luo, B. Shen, J. Alloys Compd. **790**, 633 (2019).
[23] K.K. Song, X.F. Bian, X.Q. Lv, J. Guo, G.H. Li, M.T. Xie, Mater. Sci. Eng. A **506**, 87 (2009).
[24] M. Mansouri, N. Varahram, A. Simchi, J. Non-Cryst. Solids **506**, 46 (2019).
[25] M. Salehi, S.G. Shabestari, S.M.A. Boutorabi, J. Non-Cryst. Solids **375**, 7 (2013).
[26] J. Orava, A.L. Greer. Thermochim. Acta **603**, 63(2015).
[27] S.H. Wang, X.F. Bian, J. Alloys Compd. **453**, 127 (2008).
[28] Z. Zhou, Z. Zhang, Y. Chen, X. Liang, B. Shen, Surf. Coat. Technol. **408,** 126800 (2021).
[29] S. Zhao, H. Wang, L. Xiao, N. Guo, D. Zhao, K. Yao, N. Chen, Physica E Low Dimens. Syst. Nanostruct. **94**, 100 (2017).
[30] X.F. Wang, X.Q. Wu, J.G. Lin, M. Ma, Mater. Lett. **61**, 1715 (2007).
[31] Z. Zhou, L. Wang, X. Zhao, J. Wu, F. Zhang, J. Pi, Surf. Interfaces **23**, 100956 (2021).
[32] J. Jorcin, M.E. Orazem, N. Pébère, B. Tribollet, Electrochim. Acta **51**, 1473 (2006).
[33] R. Attias, B. Dlugatch, M.S. Chae, Y. Goffer, D. Aurbach, Electrochem. Commun. **124**, 106952 (2021).
[34] S. Lu, K. Yao, Y. Chen, M. Wang, N. Chen, X. Ge, Corros. Sci. **103**, 95 (2016).
[35] A. Sotniczuk, D. Kuczyńska-Zemła, A. Królikowski, H. Garbacz, Corros. Sci. **147**, 342 (2019).
[36] C. Lu, Y. Lu, Z. Lai, H. Yen, Y. Lee, J. Alloys Compd. **842**, 155824 (2020).